CFD modelling of an indirect thermocline energy storage prototype for CSP applications

CFD modelling of an indirect thermocline energy storage prototype for CSP applications

Mattia Cagnoli[1], Walter Gaggioli[2], Raffaele Liberatore[2], Valeria Russo[2], and Roberto Zanino[1,*]

[1] *Dipartimento Energia, Politecnico di Torino, Corso Duca degli Abruzzi 24, 10129 Torino, Italy*
[2] *ENEA, Centro Ricerche della Casaccia, 00123 Roma, Italy*

*corresponding author: roberto.zanino@polito.it

Abstract

Thermocline thermal energy storage is a (potentially) cost-effective alternative to the more widespread two-tank solution, as both the hot and the cold medium are stored in a single tank.
An innovative thermocline technology was recently developed by ENEA and a prototype was experimentally tested at the Casaccia laboratories. The storage tank is equipped with two flat-coil heat exchangers (HXs) located at the bottom and at the top of the tank, for the charge and discharge phases, respectively. An internal vertical channel, which assists the motion of the storage medium (a mixture of molten salt) during the charge and discharge transients, connects the two HXs.
In this paper, a detailed, transient 2D axisymmetric Computational Fluid Dynamics (CFD) model of the prototype has been developed. The model simulates the charge and discharge transients, determining the heat losses and the temperature distribution of the molten salt in the tank. The computational domain includes the storage medium, the tank insulated walls and the main components immersed in the molten salt, i.e., the heat exchangers and the vertical channel.
The model has been first calibrated by best-fitting the data measured during a test conducted without any thermal load, then validated against another independent set of experimental data.
A first comparison against a charge transient showed some discrepancies between the computed and the measured temperatures of the salt, which could be explained by assuming the presence of a bypass at the location of the HXs. This assumption is discussed and justified in the paper. The CFD domain has then been modified to include the bypass, and this allowed to successfully validate the model against experimental data in both charge and discharge phases.
The validated model is finally exploited to assess how a variation in the diameter of the internal vertical channel could affect the thermal performance of the storage system in a charge transient. The results indicate that decreasing the channel diameter leads to an increase of the salt temperature at the very top of the tank at the cost of a longer time to fully charge the storage.

Keywords: Concentrated Solar Power (CSP), Thermal Energy Storage (TES), Thermocline, CFD

1 Introduction

Climate change imposes rethinking the way to produce electricity replacing fossil sources with renewable energy sources that do not contribute to the emission of greenhouse gases. Among the renewables, concentrated solar power (CSP) technology has a great potential to play a relevant role in the energy transition.
This technology exploits the abundant solar resource, which exceeds several times the world energy demand (World Energy Council, 2013), by using a set of mirrors (the so-called solar field) to concentrate the solar beams on a receiver where the solar energy is converted into enthalpy increase of a heat transfer fluid (HTF). The thus collected energy can be directly used to produce electricity, or it can be stored in a thermal energy storage (TES), which allows decoupling the electricity production from the intermittent solar resource, making the former dispatchable. This is a key and well-known asset of CSP, since both wind and photovoltaic power generation systems, i.e., the two most widespread renewable energy technologies, do not allow directly storing thermal energy.

To date, the most widespread and commercially mature CSP technology is the parabolic trough, coupled with a two-tank indirect thermal energy storage (Fernández et al., 2019). In this case, the TES consists of a cold tank at the receiver inlet and a hot tank at the receiver outlet, which are filled with molten salt as a heat storage medium (HSM). This storage system is typically indirect since the HTF is commonly a synthetic oil while the storage medium is a mixture of molten salt; thus, a heat exchanger (HX) is required to transfer the heat between the HTF and the storage medium. Nevertheless, direct TES systems, using molten salt both as HTF and HSM are also being applied (Turchi et al., 2019).

An alternative TES concept is the thermocline storage system that consists of a single-tank in which the cold and the hot medium are separated by a buoyancy-driven thermal stratification. The cold fluid, having a higher density, settles on the bottom, while the hot fluid stratifies on the top; the region between these two layers is characterized by a thermal gradient that is called "thermocline". The thermocline TES is considered an attractive alternative to the more widespread two-tank configuration since it requires only a single tank; according to the literature, it potentially allows reducing the investment cost up to 30% (Gaggioli et al., 2014; Pacheco et al., 2002). However, the thermocline storage system suffers of a lower thermal performance, i.e. of a non-purely two-temperature system, with respect to the two-tank configuration (Angelini et al., 2014), because the thermal gradient established between the cold and the hot fluid implies an exergy destruction due to the mixing between the fluids at different temperatures (Rosen, 2001). The thicker the thermocline (i.e. the mixing region) the lower the thermal performance at equal tank height.

Different numerical and experimental studies were conducted in the past on the thermocline TES system. Xu et al. (Xu et al., 2013) developed a transient 2D thermal fluid dynamic model of a packed-bed molten salt thermocline thermal storage system. They showed that the particles' diameter significantly influences the heat transfer between the solid particles and the molten salt: the larger the diameter the lower the heat transfer rate.
Angelini et al. (Angelini et al., 2014) numerically analyzed the thermal performance of a molten salt thermocline filled with quartzite. A 2D finite element model was developed, which computes the temperature distribution in the tank. The results indicate that the tank size affects the thermal performance: a small tank allows a steep thermocline, but it is quickly fully charged; on the contrary, a large tank has a greater capacity, but it presents a lower efficiency because of the thicker thermocline. Angelini et al. concluded that also considering the best tradeoff, the storage efficiency is still about 33% lower than with the two-tank option.
Gaggioli et al. (Gaggioli et al., 2014), proposed an innovative TES concept consisting of a single tank thermocline storage system filled with a mixture of nitrate salts that works both as HSM and as HTF in the solar field. The tank is equipped with an integrated helically coiled steam generator that allows producing steam at the required quality. The integrated steam generator aims at making the CSP system more compact while reducing the investment cost. The experimental tests conducted at the ENEA PCS facility have confirmed the technical feasibility of the proposed concept.
Pizzolato et al. (Pizzolato et al., 2015) developed a CFD-assisted, system-level model of the single-tank thermocline storage system with an integrated steam generator as proposed in (Gaggioli et al., 2014). A set of CFD simulations was performed to characterize the system-level model of the thermocline, which thus maintains approximately the same accuracy as the validated CFD model, but with a dramatically reduced computational cost making the model suitable for annual performance analysis. The whole system-level model of the CSP plant, based on the parabolic trough technology and including the single-tank thermocline storage system with an integrated steam generator, is presented in (Pizzolato et al., 2017). The main conclusion was that the system proposed could generate electricity in middle Italy with a 15% cost reduction compared to the two-tank option.
Abdulla and Reddy (Abdulla and Reddy, 2017) proposed a transient, 2D, two-phase numerical model to investigate the thermal performance of a packed-bed thermocline TES system. The results of this numerical study showed that the operating temperature difference between the bottom and the top side of the tank has a significant impact on thermal performance; particularly, increasing the temperature difference leads to a reduction in efficiency.
Elfeky et al. (Elfeky et al., 2019) performed a parametric study to optimize the values of latent heat and melting temperature of multilayered phase change materials (PCMs) in a molten salt thermocline TES. The bed region was filled with spherical capsules containing PCMs characterized by different thermo-physical properties. The numerical model adopted for the parametric study is based on the Dispersion-Concentric equations and the main conclusion of this study is that three layers of PCMs are required to obtain the best performance.
Elsihy et al. (Elsihy et al., 2020) developed a transient 2D non-equilibrium thermal model to investigate the simultaneous charging and discharging performance of a molten salt packed-bed thermocline. Three different filler materials (quartzite rock, slag pebbles, and alumina ceramics) were considered and compared with the case of a pure

molten salt tank. The results indicate that a pure molten-salt tank achieves better thermal stratification than a packed-bed tank during the stable charging operation.
Recently, Palomba and Frazzica (Palomba and Frazzica, 2022) published a review of the numerical methods for the design of thermocline TES observing that only a few models are experimentally validated. The numerical methods have been classified on the base of the dimensionality (simple 1D or more accurate 2D models) and the number of phases.

The present work deals with an innovative single-tank (pure) molten salt indirect thermocline TES, which was proposed by ENEA within the ORC-Plus project (ENEA, 2020; Falchetta, 2017). This TES technology is suitable for CSP plants of medium-small size (1-5 MWe) working at medium-low temperatures; particularly, it was designed to be coupled with a Linear Fresnel Collector (LFC) solar field and with a power block based on the Organic Rankine Cycle (ORC). A prototype of such thermocline was realized and tested by ENEA at the Casaccia research centre (Gaggioli et al., 2020); Figure 1 shows a picture of the 200 kWh prototype.

Figure 1. The prototype of the thermocline storage system proposed by ENEA and installed at the PCS facility of ENEA Casaccia (Gaggioli et al., 2020)

The salt mixture (HITEC XL) fills about 93 % of the prototype tank height, and the remaining part of the tank (above the salt) is filled with air at atmospheric pressure that is ensured by an open flange on the tank roof.
The main novelty of the proposed concept is the presence of a thermally insulated internal vertical channel (4" diameter). The purpose of the internal channel is to assist the buoyancy-driven motion of the salt in order not to perturb the thermal stratification in the body of the tank, potentially leading to a thinner thermocline and, therefore, to better thermal performance.
At the channel ends, two helically coiled serpentine HXs are located, installed in a non-insulated shell, for the charge and discharge phase respectively. The charge (bottom) HX consists of 4 parallel serpentines having 28 loops each; the discharge (top) HX consists of 6 parallel serpentines having 28 loops each. The HTF, which is a mineral oil (Delcoterm Solar E15), flows in the two HXs immersed in the molten salt. During the charge phase, see Figure 2a, the charge HX heats the cold salt which flows in the shell, pushing it upwards along the vertical channel because of buoyancy forces. Similarly, during the discharge phase, see Figure 2b, the discharge HX cools down the hot salt, which flows downward through the channel because of the increased density. In the tank body, the salt is almost at rest because of the mass conservation law, being the tank cross section much higher than that of the channel.
A thermal insulation layer is applied on the tank outer wall to minimize the heat lost to the environment. The insulation material adopted is Rockwool in the vertical and bottom walls of the tank, while the top wall and the internal channel adopt Cerablanket.

In this paper, a detailed CFD numerical model of the prototype is developed and validated against experimental data; the model aims at identifying the thermal-fluid-dynamics mechanisms that affect the storage efficiency, in order to develop design solutions able to improve the thermal performance of the thermocline. The work is based on the preliminary CFD study conducted by Ivan Pellegrino as part of his MSc thesis at Politecnico di Torino (Pellegrino, 2020).

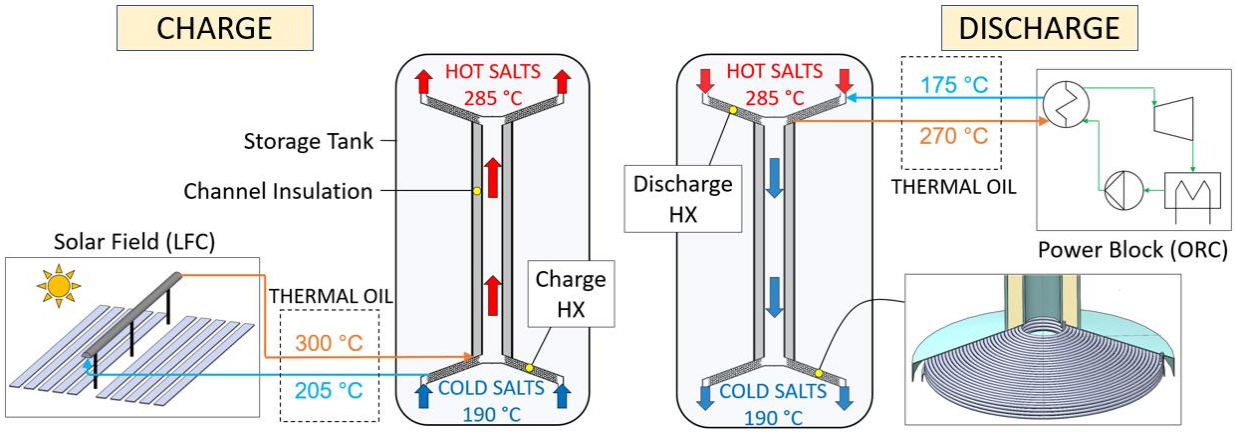

Figure 2. Operating principle of the single-tank molten salt thermocline TES equipped with two helically coiled HXs connected by a vertical channel: (a) charge phase driven by a LFC solar field and (b) discharge phase that feeds an ORC-based power block. The inset shows a zoom of the charge HX at the tank bottom

The paper is organized as follows: the experimental set-up of the thermocline TES prototype is described in section 2 and the results of the experimental campaign relevant for the present study are summarized in section 3. The CFD model of the TES prototype is presented in section 4; this section also presents the geometric simplifications introduced to have an axisymmetric domain, which are compensated by an ad-hoc calibration procedure (section 5). In section 6, the CFD model is first compared against the experimental data collected during a charge test; this comparison suggests the presence of a bypass at the HXs location. Then, the CFD model is validated against an independent set of charge and discharge experimental data. As a first application of the CFD model, we then present in section 7 a parametric assessment of how the vertical channel diameter affects the TES thermal performance. Finally, conclusions are provided in section 8.
This work has been very recently presented at SolarPACES 2022 in Albuquerque (NM).

2 Experimental set-up

Figure 3a provides a sketch of the prototype. The prototype is equipped with a couple of electrical heaters that allow for compensating heat losses during the idle time, as well as achieving the desired temperature before the beginning of the test. According to (Gaggioli et al., 2020; Liberatore et al., 2019), the experimental set-up includes:

- an electrical heater to simulate the solar field during the charge phase, i.e., a LFC system working in the oil temperature range of 205-300 °C;
- an air cooler that simulates the power block during the discharge phase. The considered power block is an ORC with design oil inlet and outlet temperatures equal to 175 °C and 270 °C, respectively.

The diagnostics installed in the TES to assess the thermal performance of the prototype are (see Figure 3b):

- 12 equally spaced thermocouples along the vertical direction, all at the same azimuthal angle, to measure the thermal gradient in the thermocline. The distance between two adjacent thermocouples is about 0.2 m; the distance between the first thermocouple and the tank floor is not known and is assumed equal to 0.1 m in this study. The distance between these thermocouples and the tank axis is 0.44 m
- 2 thermocouples spaced at 180° apart and located at the channel top and bottom ends to measure the salt temperature at the inlet/outlet of the HXs
- 1 thermocouple installed at the inlet/outlet of the HXs to measure the oil temperature increase/decrease (discharge/charge phase, respectively) due to the heat transferred in the heat exchanger serpentine
- 1 flow meter installed on the oil circuit.

The thermal power provided or removed by the HXs during the tests is deduced from the oil energy balance given the measured oil inlet/outlet temperature and mass flow rate. Similarly, the salt mass flow rate in the channel is obtained indirectly by means of the power balance

$$\dot{m}_{salts} = \frac{\dot{m}_{oil} \int_{T_{oil,in}}^{T_{oil,out}} c_{p,oil}(T_{oil}) dT}{\int_{T_{salts,in}}^{T_{salts,out}} c_{p,salts}(T_{salts}) dT} \quad (1)$$

where $\dot{m}$ is the mass flow rate, T is the temperature and c_p is the specific heat. The subscripts *oil* and *salt* indicate which medium is considered, while *in* and *out* correspond to the inlet/outlet, respectively. This approach is applicable with good approximation only in the phases of the transient which are close to steady state (see below).

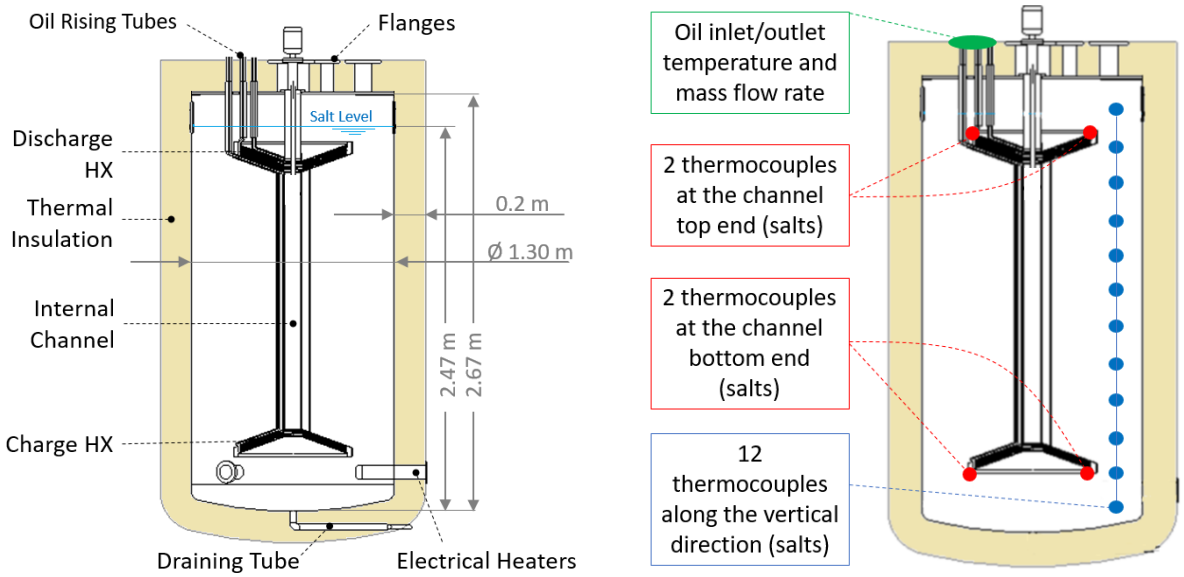

Figure 3. (a) Sketch of the thermocline-based thermal energy storage prototype developed by ENEA with the tank dimensions and (b) diagnostics adopted to experimentally assess the thermal performance

3 Selected experimental data

The experimental campaign aimed at validating the feasibility of the prototype concept was conducted at the ENEA PCS facility in January 2019. Gaggioli et al. (2020) describe the tests and the main results obtained.
The experimental campaign consisted of 7 discharge tests, 3 charge tests and 1 test without any thermal load; the data was collected with a sample time of 5 seconds.

In this study, the results of the experimental campaign have been exploited first to calibrate the heat lost from the tank boundary to the environment, by considering the test performed in the absence of thermal load (section 5), then to validate the newly developed dynamic numerical model against both charge and discharge transient tests (section 6). For this purpose, portions of charge and discharge tests where the thermal load is almost constant have been selected. The condition of almost constant heat load is adopted to minimize the error made adopting the steady-state approximation for the estimation of the salt mass flow rate (Eq. 1). The finally chosen tests, which satisfy the aforementioned criterion, are summarized in Table 1 that also includes the test conducted in the absence of any thermal load.

Table 1. List of the tests considered in this study for comparison with the numerical model. The selected portion of the test, in terms of start/end time, is also indicated

Test ID	Type of test	Date	Start time	End time
L1	No Thermal Load	January 22, 2019	0 min	208 min
C1	Charge	January 24, 2019	80 min	120 min
C2	Charge	January 28, 2019	30 min	174 min
D1	Discharge	January 17, 2019	80 min	95 min

Figure 4 shows the salt temperature evolution at different heights from the tank bottom during the test portions considered, except for the test with no thermal load. In the first charge test, see Figure 4a, the salt temperature increase is modest and involves all the tank layers; this is not desired in a thermocline TES, where the aim is to heat up only the salt on the top layers. In the second charge test (Figure 4b), the temperature of the salt progressively increases starting from the very top layer; however, the temperature of the first 3 layers on the bottom immediately increases with no delay. This is likely because the charge HX loses some heat towards the shell heating the salt at the bottom. The temperature measured by the lowest thermocouple in both charge tests considered here is very low, indicating that probably the salt at the tank bottom is nearly frozen (the melting process starts at about 120 °C (Gomez et al., 2013)). The discharge test (Figure 4c) shows that the salt temperature of the top layers progressively decreases reaching the temperature of the cold salt at the tank bottom. The discharge transient does not last long enough to cool down the salt layers at the very top of the tank.

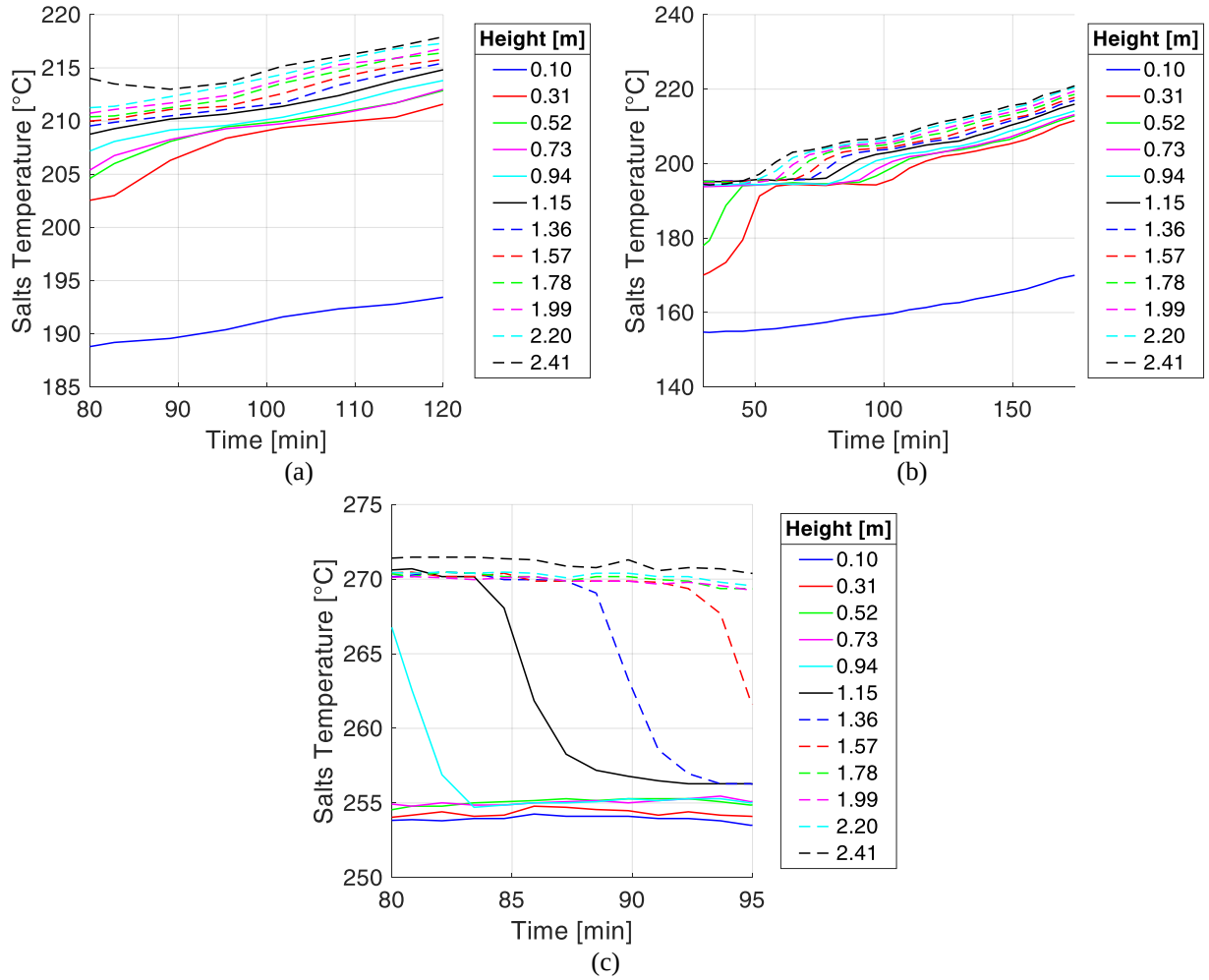

Figure 4. Salt temperature evolution measured by the 12 thermocouples located at different heights along the tank vertical direction during the charge tests (a) C1, (b) C2 and the discharge test (c) D1.

4 CFD model

This section presents the dynamic 2D CFD model of the thermocline prototype that aims at accurately estimating the salt temperature distribution in the storage tank during charge and discharge transients. The model has been developed using the commercial software Star-CCM+ (Siemens, 2021).

4.1 Computational domain and boundary conditions

The 2D (axisymmetric) computational domain is shown in Figure 5. It includes the molten salt, the air layer above the salt, the metal walls (AISI 316) and the thermal insulation layers. The computational domain ends at the outer surface of the HXs tubes; thus, it does not include the oil flow.
The 2D approach is commonly adopted in similar studies (Pizzolato et al., 2015; Rivas et al., 2014) since it allows reducing the computational cost without significantly affecting the accuracy of the results. The latter statement is justified since the thermal load is almost axisymmetric, and provided the geometry of the storage tank can also be approximated as such, which requires introducing some minor geometrical simplifications as follows:

- the support structures of the tank are not considered. This implies neglecting the thermal bridges related to these structures; therefore, if uncompensated, the model would tend to underestimate the heat losses;
- the electrical heaters in the tank have been removed since they are switched off during the charge and discharge transients; moreover, they occupy a very limited share of the tank volume;
- the oil tubes that connect the HXs with the oil circuit have been removed because they are thermally insulated (the heat transfer with the salt is negligible) and because they occupy a very small share of the tank volume;
- the flanges on the tank roof are removed, apart from that open toward the environment, which has been moved from the original position to the axis of the tank. The removed flanges would also constitute neglected thermal bridges and, therefore, further underestimated heat losses.

To compensate the neglection of the thermal bridges associated to the support structures and the flanges, the thermal conductivity of the insulation layers has been calibrated ad-hoc, in a way that best fits the results of the test performed with no thermal load, see section 5 below.

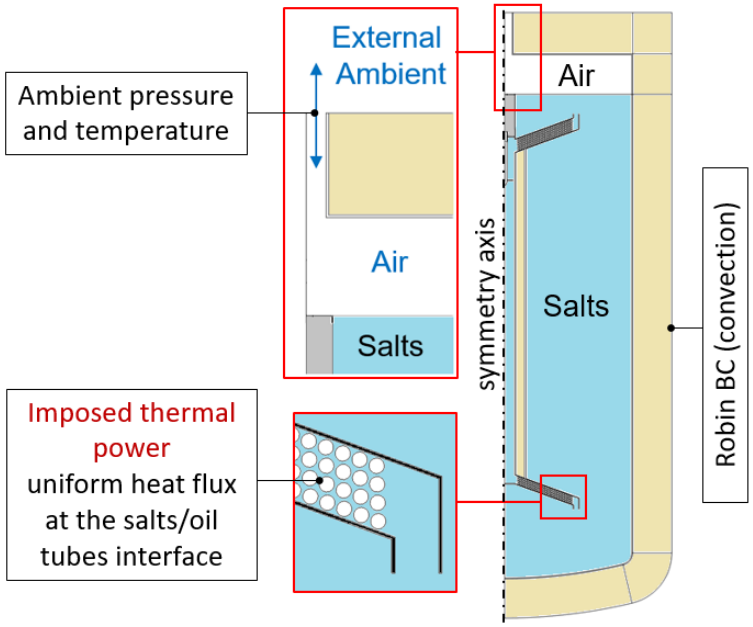

Figure 5. Computational domain (axisymmetric) and boundary conditions. The insets show zooms of the region of the charge HX (bottom) and of the region of the open flange (top).

The CFD model includes gravity, which is the driver of the buoyancy forces responsible for the salt movement in thermal storage. The SST k-ω turbulence model is adopted, which allows taking into account the mixing of the salt within the tank (Pizzolato et al., 2015).
The applied boundary conditions applied are summarized in Table 2.

Table 2. Boundary conditions

Surface	**Boundary Condition**	**Notes**
Active HX	Imposed thermal power removed from or provided to the salt	The active HX depends on the phase (charge/discharge)
Inactive HX	Adiabatic	
Top (flange) opening	Ambient pressure and temperature	
External tank	Ambient temperature and heat transfer coefficient (Robin BC)	Suitable correlations introduced for the heat transfer coefficient, according to Eq. 2 and 3

The heat lost by convection towards the environment is computed using the Newton's law of cooling as a function of the imposed ambient temperature and by introducing a suitable heat transfer coefficient based on correlations available in the literature. The Churchill & Bernstein correlation (Eq. 2), which is suitable for cylinders in crossflow, is adopted for the lateral (vertical) side of the tank (Incropera et al., 2012)

$$Nu = 0.3 + \frac{0.62 Re^{1/2} Pr^{1/3}}{(1 + (0.4/Pr)^{2/3})^{1/4}} \left(1 + \left(\frac{Re}{282000}\right)^{5/8}\right)^{4/5} \quad (2)$$

where Nu is the Nusselt number, Re and Pr are the Reynolds and Prandtl numbers respectively. On the top and bottom side, a correlation suitable for horizontal plates in parallel flow is considered (Incropera et al., 2012); see Eq. 3, where Re_c is the critical Reynolds number that identifies the transition from laminar to turbulent.

$$Nu = \left(0.037 Re^{4/5} - 0.037 Re_c^{4/5} + 0.664 Re_c^{1/2}\right) Pr^{1/3} \quad (3)$$

Radiative heat losses have been neglected because convection is expected to dominate the heat transfer with the environment, being the temperature of the tank external surface relatively close to the ambient temperature, as it can be estimated by means of a simple hand calculation.

4.2 Space and time discretization

A polygonal mesh has been adopted, which is suitable in the case of complex geometries as in the region of the heat exchangers. The mesh has been refined by employing 3 prism layers on the HXs tube walls to accurately solve for both the flow and the temperature fields. About 10^5 cells are enough to ensure mesh independent results. Figure 6 provides a view of the adopted mesh with the detail of the region close to the HXs.
Regarding time discretization, a time step of 2 seconds with 100 iterations per time step is a good compromise between the accuracy of the results and the computational time, according to a time step independence study.

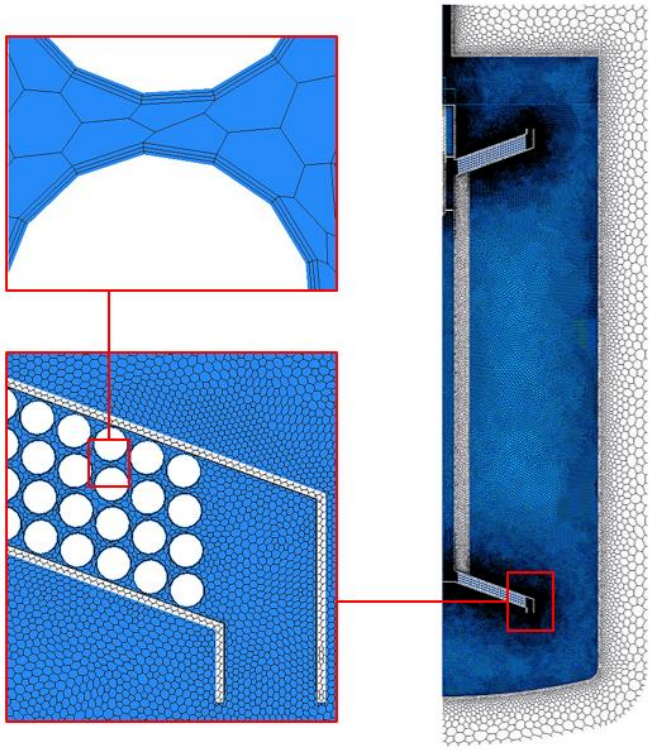

Figure 6. Computational mesh. Insets show successive zooms on the bottom HX region.

5 Ad-hoc calibration of the tank wall heat conductivity

The simplifications introduced in the geometry (see section 4.1) make the calibration of the thermal conductivity of the tank insulation layer necessary to account for the thermal bridges, which have been neglected (top flanges and support structures). For this purpose, the experimental test conducted in the absence of thermal load is considered (L1 in Table 1). In this test, the salt was heated up to an almost uniform temperature, equal to about 264 °C, then the thermal load was switched off and the salt started cooling down due to the heat losses for 3.5 hours. The CFD model has been set to reproduce this test, imposing a uniform initial temperature (264 °C), and disabling the thermal driver. The ambient temperature has been assumed to be 7 °C and the wind speed to 7 m/s, which are average values for January at the test facility site. The wind speed allows determining the Reynolds number in Eq. 2 and 3. It has been checked that varying the ambient temperature and the wind speed does not affect the results of the simulation in a significant way.

Figure 7 shows the calibration result: the salt temperature evolution computed with the CFD model is in good agreement with the experimental measurements. To obtain this result, the thermal conductivity of the tank insulation layer has been modified starting from a preliminary estimation, which was based on a surface-averaged calculation of the equivalent thermal conductivity obtained replacing the area of the geometric elements removed with stainless steel. The imposed value for the bottom and lateral side is 0.35 W/mK instead of 0.09 W/mK (Rockwool), while for the top part a thermal conductivity of 1.5 W/mK is imposed instead of 0.06 W/mK (Cerablanket). The remarkable increase in the thermal conductivity of the top part is due to the presence of the flanges, which determine large thermal bridges that significantly increase the heat losses

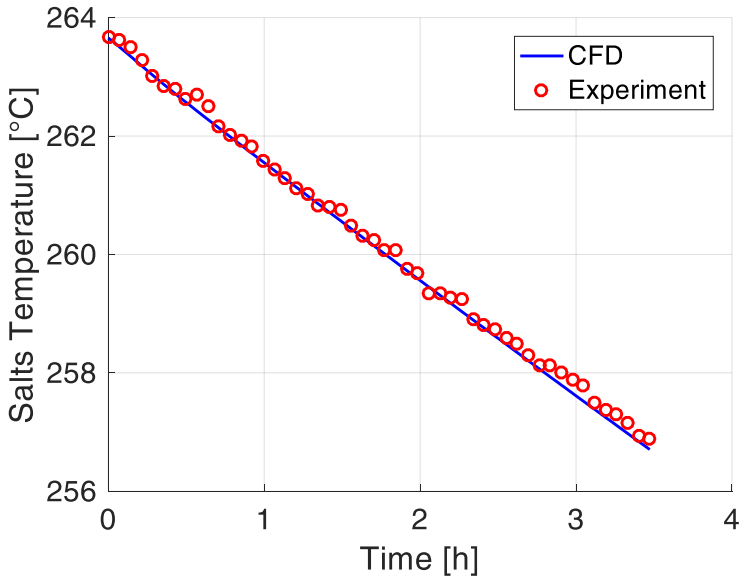

Figure 7. Calibration of the thermal conductivity of the tank insulation layer: computed salt temperature evolution in the absence of thermal load, against experimental data

6 Comparison against experimental data from charge and discharge tests

This section presents the calibration and validation of the CFD model against the charge and discharge tests reported in Table 1. The computed thermal stratification in the tank at the end of the transient is compared against the experimental values. First, the model is best-fitted against the charge test C1. The discrepancy initially obtained between the computed and the measured thermal stratification suggests the presence of a bypass at the HXs, which indeed allows reproducing the experimental data, as explained in section 6.1. Then, the calibrated model with the bypass is validated against the charge test C2 and the discharge test D1.

6.1 Ad-hoc calibration of the model against data from the charge test C1

According to Table 1, two sets of experimental data are available for the validation of the CFD model in the charge phase. First, test C1 is considered to calibrate the CFD model. For this purpose, the model has been set to reproduce the test conditions, applying proper initial and boundary conditions. The former mainly consists of defining the initial temperature and velocity of the molten salt as follows:

- molten salt temperature: the thermal stratification measured at the test initial time is imposed along the axial direction, assuming the no thermal gradients occur along the radial direction;
- molten salt velocity: in the vertical channel, the velocity is imposed equal to the estimated value from the test (Eq. 1), assuming that only the axial component exists. In the tank body, the velocity is assumed equal to zero.

The boundary conditions have been imposed according to Table 2; the thermal power measured during the experiment is imposed on the surface of the active (charge) heat exchanger, assuming a uniform heat flux distribution on the HX surface. The monthly-averaged ambient temperature (7 °C) and wind speed (7 m/s) during the period of the experimental campaign have been considered to define the boundary condition on the tank outer side.

According to Figure 8 (no bypass case), the computed salt temperature distribution along the vertical direction is rather different from that measured by the thermocouples during the experiment. Nevertheless, the average salt temperature is practically the same; this is because the stored thermal energy is about the same as it was expected since the thermal power is imposed according to the test data and the heat losses have been calibrated (section 5).

The reason for the different temperature distribution has been identified in the computed mass flow rate in the channel, which is about 6 times lower than the experimental estimation (Eq. 1), resulting in a higher temperature of the salt passing through the charge HX, which then stratifies on the top of the tank.
The reason for the discrepancy in the mass flow rate could be attributed to one or more of the following causes:

1. overestimation of the mass flow rate deduced from the experiment, because of the overestimation of the heat provided to the molten salt by the oil, which appears at the numerator of Eq. 1. In fact, the oil temperatures were measured outside of the tank and part of the heat could have been lost in the path between the tank boundary and the thermocouple;
2. inadequacy of the CFD model to reproduce buoyancy-driven phenomena accurately;
3. differences between the geometry assumed and implemented in the CFD model of the tank prototype and the actual geometry. This hypothesis could be reasonable since the CFD model is based on the design drawings, while the final constructive drawings are unfortunately not available to the authors.

Regarding the first point, the experimental data have been checked. The thermal power measured on the oil circuit has been compared against the thermal power received by the molten salt during the test, which can be deduced from the temperatures measured by the thermocouples inside the tank. This comparison resulted in an almost perfect match between the two energy balances during the transient; therefore, item 1 above can be discarded as a possible cause of the discrepancy in the mass flow rate.
For what concerns the second point, the CFD model has been successfully benchmarked (not shown) against a simplified CFD model developed by ENEA as part of the ORC-Plus project (Falchetta et al., 2017). The two models differ in the computational domain: the ENEA model includes only the molten salt in the computational domain, assuming no heat losses through the boundaries. Therefore, in order to make a fair comparison between the results of the two models, the Robin boundary condition applied on the external tank surface (see Table 2) has been replaced with an adiabatic condition. The benchmark case with the ENEA model consisted in a charge transient of 3800 s, with an imposed constant thermal power equal to 6.25 kW, since for this case of study the results obtained with the ENEA model are available. Therefore, the CFD model should not be responsible, at least not entirely, for the discrepancy with the experimental data.
As a consequence, only the third point is left as a possible cause of (most of) the discrepancy between the computed and the experimentally estimated mass flow rate in the vertical channel. Here we make the (temporarily ad-hoc) assumption that a bypass exists, providing the salt with a preferential path concerning the path around the serpentine of the HXs, resulting in a reduced total pressure drop and, consequently, a higher mass flow rate. We assume that the bypass is related to the fact that the serpentines are not perfectly bounded by the shell, but a certain gap exists between the serpentine and the shell connected with the channel, as shown in Figure 9. This hypothesis might be realistic, because the assembly of the serpentines inside the shell was the most uncertain phase of the prototype construction, as confirmed by the team that dealt with the commissioning of the thermocline (private communication).
The size of the gap between the shell and the serpentine has been best-fitted by exploiting the data of the test C1, and it turns out that a gap of 23 mm leads to a much better agreement with the experimental data, see again Figure 8 (bypass case). To quantify the difference between the computed and the experimental curves, the coefficient of determination (R^2) has been calculated, which provides an estimation of the model effectiveness in reproducing the observed data. R^2 may range between 0 (bad data reproduction) and 1 (perfect data reproduction), and for the case considered here the agreement is acceptable ($R^2 \approx 0.92$).

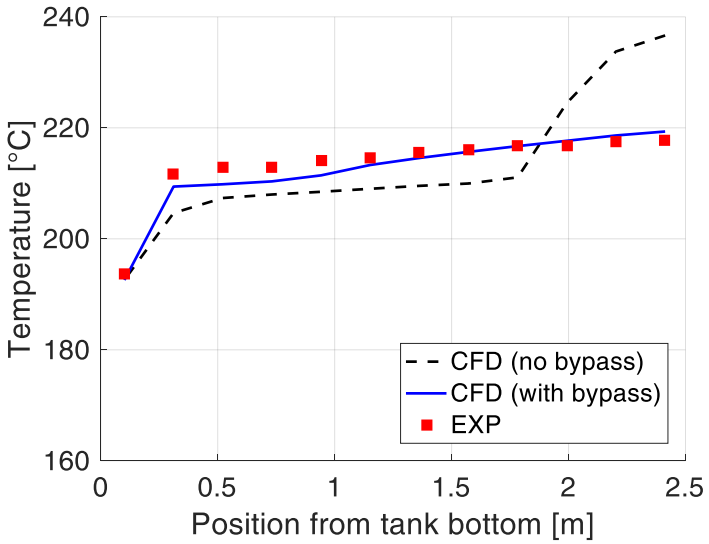

Figure 8. Salt temperature distribution along the vertical direction (from the tank bottom): comparison between experimental data (red squares) and values computed with the CFD model without and with the bypass (black dotted line and blue solid line, respectively), during the C1 experiment

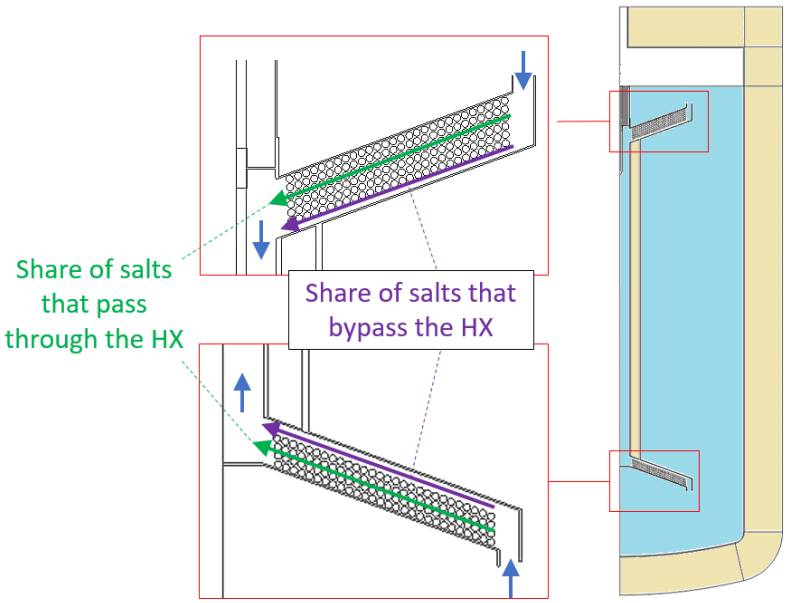

Figure 9. Thermal storage tank with a bypass assumed at the charge and discharge HXs, providing a parallel, low-impedance path, with respect to the path around the serpentine pipes.

Figure 10 shows the computed flow field and temperature distribution in the whole domain at the end of the transient, once introduced the bypass at the HXs. The channel assists the motion of the heated salt from the tank bottom to the top, while the speed of the salt in the tank body remains close to zero. This means that the salt heated by the charge HX rises in the vertical channel stratifying on the top of the tank without perturbing the temperature gradient in the tank body. However, as visible also in Figure 8, the presence of the bypass makes this gradient almost flat.
Part of the heat provided by the charge HX is transferred through the shell leading to a temperature increase in the salt surrounding the shell. The salt heated under the shell are trapped by the channel itself (see Figure 10b), they cannot reach the top part of the tank, and, for this reason, they do not contribute to charge the tank. Figure 9 also shows some vortices generated in the air layer over the molten salt free surface, which are caused by the temperature gradient between the salt surface and the colder internal tank surfaces. In principle, the vortices enhance the convective heat transfer, increasing the heat removed from the salt. However, the air is almost confined in an insulated space, being

the air circulation towards the top aperture very limited; therefore, the thermal power dispersed towards the salt free surface at the end of the transient is relatively modest.

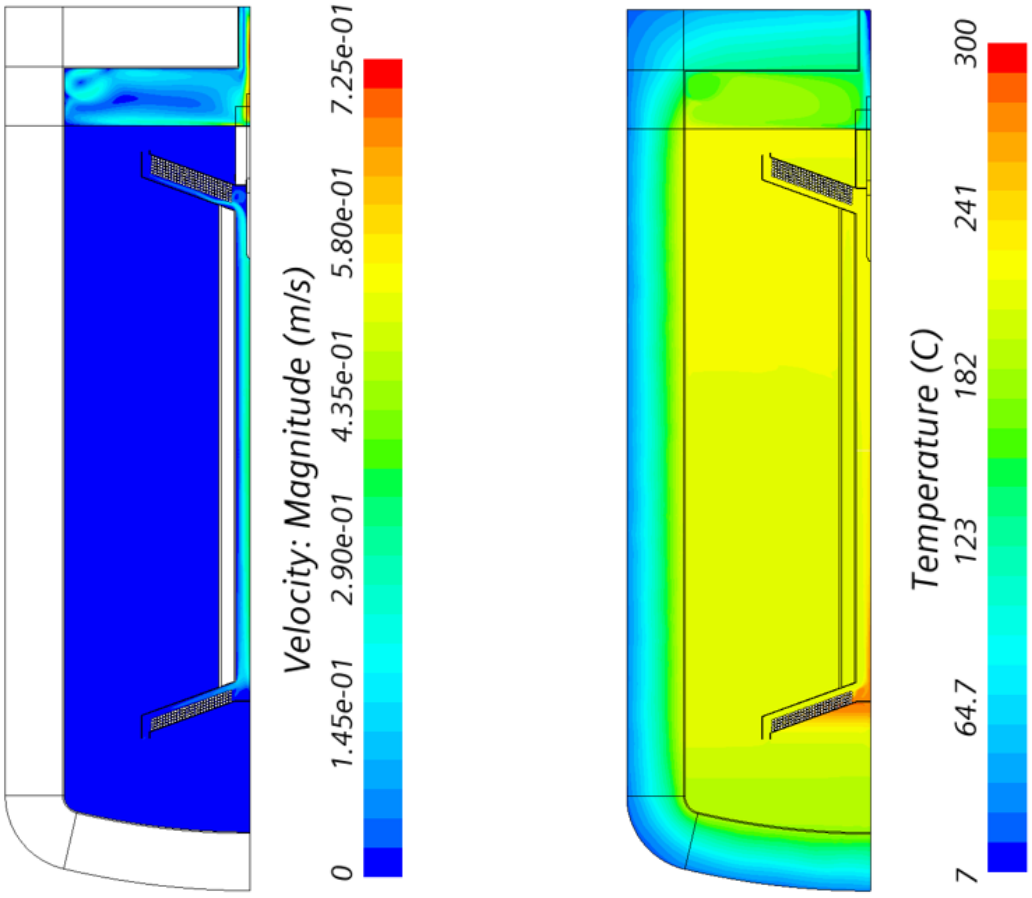

(a) (b)

Figure 10. Computed (a) speed in the salt and air regions and (b) temperature distribution in the entire domain at the end of the charge transient C1

6.2 Validation of the model against data from the charge test C2

Considering the presence of the bypass at the HX location, as discussed in section 6.1, the CFD model has been validated against the experimental measurements collected in test C2; the result of this comparison is visible in Figure 11, which indicates a good agreement between the experimental data and the computed results, in terms of salt temperature stratification ($R^2 \approx 0.94$) and salt temperature at the channel bottom and top end. The experimental measurement of the salt temperature at the channel ends is collected by means of 2 (180° displaced) thermocouples for each side (see Figure 3); the average value is considered here for each side, but the values measured are very close each other.

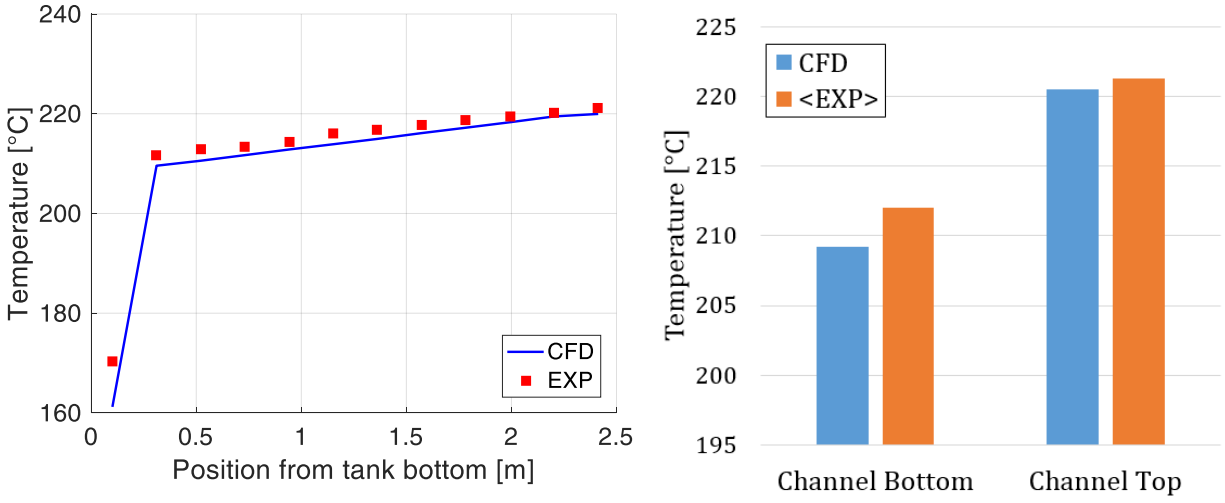

(a) (b)

Figure 11. Comparison between experimental and numerical results with the modified geometry in the C2 test: (a) salt temperature distribution along the vertical direction (from the tank bottom) and (b) salt temperature at the channel bottom and top end

6.3 Validation of the model against data from the discharge test D1

The thermal driver is applied in this case on the discharge (top) heat exchanger and consists of the thermal power removed by the oil during the transient. The modified storage tank, with a 23 mm gap between the serpentines and the shell, is considered here as well, frozen on the base of what was discussed in section 6.1.

Figure 12a shows the comparison between the computed and the experimental temperature stratification in the tank, which results in an acceptable agreement ($R^2 \approx 0.93$). The same conclusion is obtained looking at Figure 12b that compares the measured and the computed salt temperature at the channel ends. The validation in this transient, which is very different from the C1 test used to calibrate the model, provides a good confidence in the CFD model results.

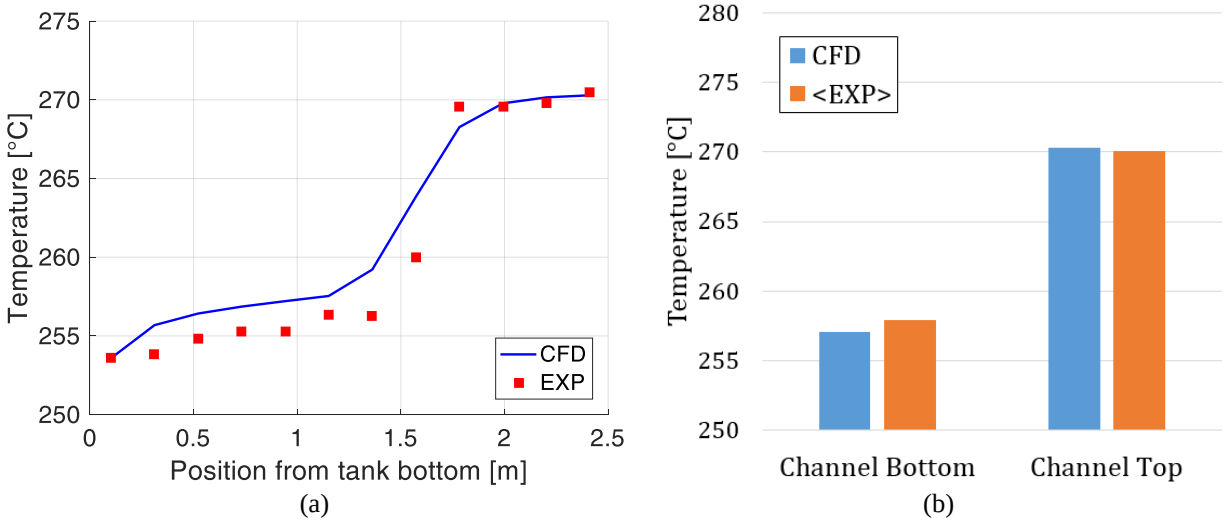

(a) (b)

Figure 12. Comparison between experimental and numerical results with the modified geometry in the D1 test: (a) salt temperature distribution along the vertical direction (from the tank bottom) and (b) salt temperature at the channel bottom and top end

7 Impact of the internal vertical channel diameter on the thermocline

In this section, a first application of the validated CFD model is presented: the diameter of the internal vertical channel is parametrically varied to assess how it affects the thermocline formation. For this purpose, the charge test C1 is considered and the channel diameter is progressively reduced. This leads to an increase of the pressure drop and, consequently, a decrease of the salt mass flow rate in the channel. Because of the mass flow rate reduction (at equal heat load), the salt temperature is expected to increase, leading to better thermal stratification.
This study aims at exploring the thermal performance potential of the thermocline as originally designed by ENEA, i.e., without the bypass. In fact, the latter has a negative impact on the storage performance and, therefore, it will not be considered in future developments of this technology.
The channel diameters considered here are 4" (the original value), 2" and 1". The reduction of the diameter is obtained by thickening the metal wall of the channel; for each geometry, a new mesh is generated.

Figure 13 shows the computed thermal stratification of the molten salt along the tank vertical direction. The storage system with an internal channel diameter of 2" presents almost the same thermal gradient as the original case, while a further halving of the diameter (from 2" to 1") determines a relevant variation in the salt thermal stratification. The variation is localized on the top layers where higher temperatures are reached leading to an increase of about 26 % of the temperature difference between the top and the bottom side of the tank.
The mass flow rate reduction in the channel is about 7.5 % and 40 % for the 2" and 1" diameters, respectively. The temperature difference across the charge heat exchanger depends mainly on the mass flow rate since the heat load is imposed, for this reason, it varies by similar percentages. The change of the salt temperature at the outlet of the charge heat exchange determines, in the end, the salt temperature distributions in the tank shown in Figure 13.

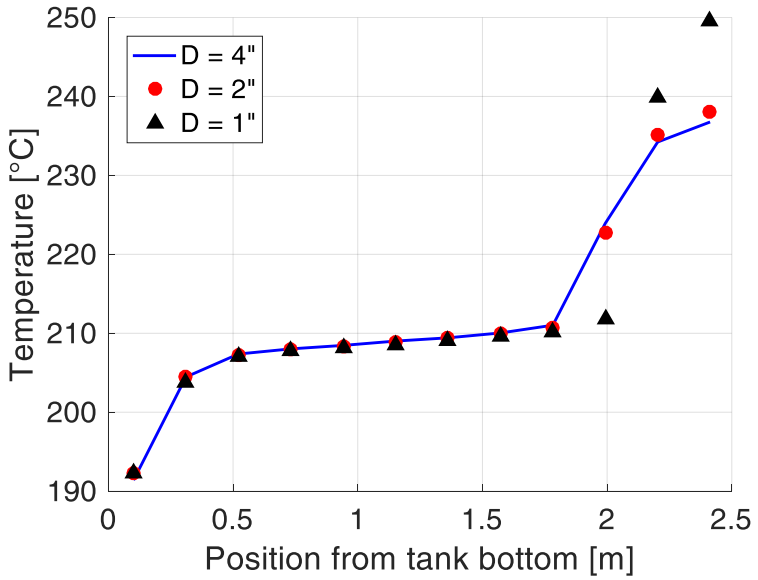

Figure 13. Salt temperature distribution along the vertical direction from the bottom of the tank for different diameters of the internal channel

Figure 14 provides the comparison between the original channel diameter (4") and the narrowest diameter considered here (1"), in terms of salt temperature evolution at different heights from the tank bottom. As observed above, the temperature of the salt at the top (height = 2.36 m ~ top end of the channel) increases reducing the diameter, because of the higher temperature of the salt rising the vertical channel. The transient dynamics is different depending on the size of the channel diameter. For a diameter of 1", the layers below the top have a slower response with respect to the original case. In fact, the smaller the diameter the lower the amount of salt passing through the heat exchanger, which will then require a longer time to replace the salt in the tank below the top layer. The latter has an almost unperturbed response because the speed of the heated salt in the channel does not change enough to really affect the response of this layer. Asymptotically, the temperature of all the layers will be higher reducing the channel diameter, in view of the reduced mass flow rate.

Therefore, decreasing the channel diameter allows for reaching higher temperatures at the cost of a longer time required to fully charge the storage system. The best tradeoff between the salt temperature and the duration of the transient is an optimization exercise that involves the connected components (receiver and power unit) and their specific operation, which is beyond the scope of the present paper.

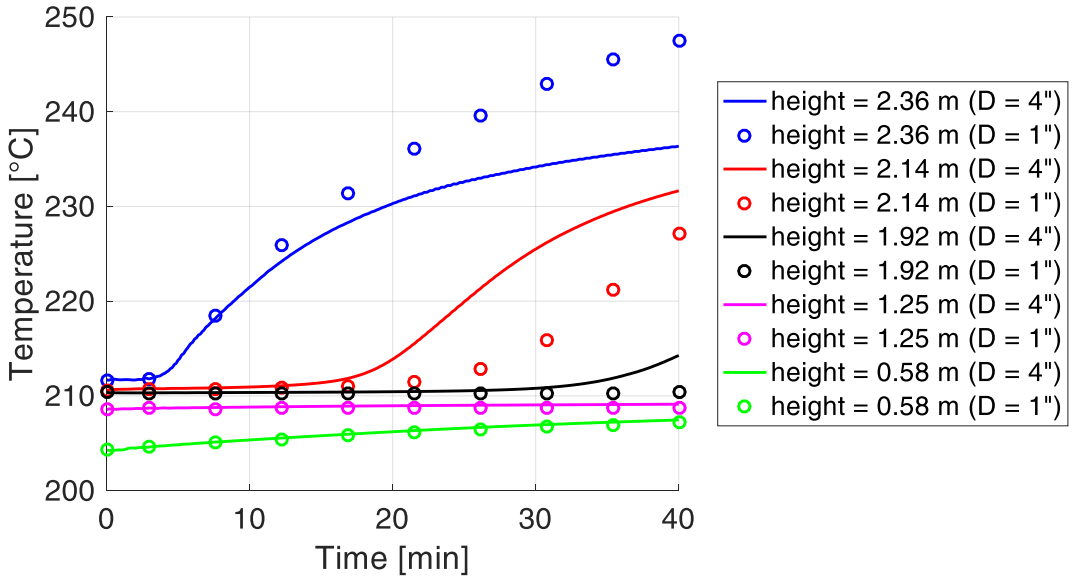

Figure 14. Salt temperature evolution during the transient at different heights from the tank bottom side: comparison between the 4" and 1" channel diameters.

8 Conclusions and perspective

This paper presents a 2D (axisymmetric) CFD model developed to accurately reproduce the charge and discharge transients of an innovative TES prototype based on the thermocline concept designed and experimentally tested by ENEA. The prototype is equipped with two flat coil HXs for the charge (bottom side) and discharge (top side) phases, respectively. An internal vertical channel connects the two HXs providing a preferential path for the salt motion.

The CFD model computes the buoyancy-driven motion of the molten salt during the charge/discharge transients, determining the salt temperature distribution in the tank, considering also the convective heat losses towards the environment. The model results have been first compared against the experimental data collected during a charge test; this comparison suggests the presence of a bypass for the salt at the HXs. The assembly of the serpentines inside the shell was indeed the most uncertain phase of the prototype construction and it is not impossible that a gap resulted between the serpentines and the shell, considering also that the final executive drawings of the prototype are unfortunately not available to the authors. The model with the bypass has been successfully validated against two independent set of experimental data, related to a charge and discharge test, respectively. The latter transient is very different from the charge test initially assumed for the first comparison (and calibration); thus, the validation in the discharge phase provides a reasonable confidence about the CFD results. Finally, the validated model is applied to perform a sensitivity analysis of a charge transient, varying the size of the vertical channel diameter. The results show that reducing the channel diameter results in higher salt temperatures at the very top of the tank; however, the time required to fully charge the storage system increases as the channel diameter decreases.

The validated CFD model also allowed reaching a deeper understanding of the phenomena affecting the prototype thermal performance. From that point of view, the main conclusions of this work are listed below:

- if a bypass at the HXs location really exists, it seriously lowers the thermal performance of the storage system, as we deduced from the comparison between numerical and experimental results. An optimized TES of this type should ensure the absence of any bypass;

- the salt layers below the channel are not involved in the buoyancy-driven motion established in the tank; for this reason, the salt temperature at the very bottom is significantly lower than in the rest of the tank. An optimized design should reduce the volume of the salt below the channel;
- during the charge phase, the salt under the shell of the charge heat exchanger is heated up. This salt is trapped at the bottom by the shell and, consequently, does not contribute to the thermal stratification. In an optimized TES, the shell of the charge HX should be redesigned to avoid this phenomenon, or it should be insulated to limit the heating of the salt under the shell;
- the diameter of the vertical channel affects the temperature reached by the molten salt in a charge transient, and the duration of the transient as well. The lower the diameter the higher the temperature, at the cost of a longer time required to fully charge the storage. The best compromise between salt temperature and duration of the transient depends on the plant specifications and the storage capacity desired.

In perspective, the thermocline storage system could be optimized on the base of what was observed in this study by:

- providing the HXs shell with thermal insulation in order to minimize the heat transferred with the salt outside the channel;
- removing the conical region under the charge HX, which traps the heated salt surrounding the shell;
- moving the charge HX closer to the tank bottom, since, in the current design, the molten salt at the very bottom is not involved in the motion driven by the natural convection.

.

The CFD model could be further exploited to characterize a system-level model, which should include the solar field and the power unit, to simulate the system operation with the aim of assisting in the sizing of the thermocline. Last but not least, an additional interesting perspective, which is currently under investigation, is to explore the potential of introducing inserts filled with phase change materials in the tank, to increase the storage capacity and stabilize the salt temperature.

Acknowledgements

This research has been partially financially supported by the Italian Ministry of Economic Development through the Research on Electric System—PTR 2019-21—Objective: Technologies—Project 1.9.
I. Pellegrino contributed to the development of a first version of the CFD model within the framework of his MSc thesis at Politecnico di Torino. Computational resources were provided by HPC@POLITO (http://www.hpc.polito.it).

References

Abdulla, A., Reddy, K.S., 2017. Effect of operating parameters on thermal performance of molten salt packed-bed thermocline thermal energy storage system for concentrating solar power plants. Int. J. Therm. Sci. 121, 30–44. doi:10.1016/j.ijthermalsci.2017.07.004

Angelini, G., Lucchini, A., Manzolini, G., 2014. Comparison of thermocline molten salt storage performances to commercial two-tank configuration. Energy Procedia 49, 694–704. doi:10.1016/j.egypro.2014.03.075

Elfeky, K.E., Li, X., Ahmed, N., Lu, L., Wang, Q., 2019. Optimization of thermal performance in thermocline tank thermal energy storage system with the multilayered PCM(s) for CSP tower plants. Appl. Energy 243, 175–190. doi:10.1016/j.apenergy.2019.03.182

Elsihy, E.S., Wang, X., Xu, C., Du, X., 2020. Numerical investigation on simultaneous charging and discharging process of molten-salt packed-bed thermocline storage tank employing in CSP plants. Renew. Energy. doi:10.1016/j.renene.2020.11.139

ENEA, 2020. ORC-PLUS Project [WWW Document]. URL https://www.orc-plus.eu/

Falchetta, M., 2017. ORC-PLUS - Deliverable 2.3 - Dynamic models of the system components.

Falchetta, M., Liberatore, R., Russo, V., Nicolini, D., Marano, D., Ebolese, A., Canneto, G., Fluri, T., Zoschke, T., Branke, R., Seubert, B., Rohani, R., Muller, R., Karl, M., Uriz, I., Rodriguez, J., 2017. ORC-PLUS Deliverable 2.3 - Dynamic models of the systems components.

Fernández, A.G., Gomez-Vidal, J., Oró, E., Kruizenga, A., Solé, A., Cabeza, L.F., 2019. Mainstreaming commercial CSP systems: A technology review. Renew. Energy 140, 152–176. doi:10.1016/j.renene.2019.03.049

Gaggioli, W., Fabrizi, F., Fontana, F., Rinaldi, L., Tarquini, P., 2014. An innovative concept of a thermal energy

storage system based on a single tank configuration using stratifying molten salts as both heat storage medium and heat transfer fluid, and with an integrated steam generator. Energy Procedia 49, 780 – 789. doi:10.1016/j.egypro.2014.03.085

Gaggioli, W., Liberatore, R., Di Ascenzi, P., Mazzei, D., Russo, V., 2020. Experimental test of characterization of an innovative thermal energy storage system based on low melting molten salt thermocline tank integrated with an oil exchanger. AIP Conf. Proc. 2303, 1–8. doi:10.1063/5.0028779

Gomez, J.C., Calvet, N., Starace, A.K., Glatzmaier, G.C., 2013. Ca(NO3)2-NaNO3-KNO3 molten salt mixtures for direct thermal energy storage systems in parabolic trough plants. J. Sol. Energy Eng. Trans. ASME 135. doi:10.1115/1.4023182

Incropera, F.P., DeWitt, D.P., Bergman, T.L., Lavine, A.S., 2012. Fundamentals of Heat and Mass Transfer, sixth. ed, Wiley.

Liberatore, R., Falchetta, M., Gaggioli, W., Mazzei, D., Russo, V., 2019. Power production of an ORC system using a stratified molten salt as thermal energy storage integrated in a CSP plant. AIP Conf. Proc. 2126. doi:10.1063/1.5117651

Pacheco, J.E., Showalter, S.K., Kolb, W.J., 2002. Development of a molten-salt thermocline thermal storage system for parabolic trough plants. J. Sol. Energy Eng. 124, 1–7. doi:10.1115/1.1464123

Palomba, V., Frazzica, A., 2022. Application of numerical methods for the design of thermocline thermal energy storage: Literature review and critical analysis. J. Energy Storage 46. doi:10.1016/j.est.2021.103875

Pellegrino, I., 2020. Thermal-Fluid Dynamic Modelling of a Thermocline Storage System for CSP Applications. Politecnico di Torino.

Pizzolato, A., Donato, F., Verda, V., Santarelli, M., 2015. CFD-based reduced model for the simulation of thermocline thermal energy storage systems. Appl. Therm. Eng. 76, 391e399. doi:10.1016/j.applthermaleng.2014.11.029

Pizzolato, A., Donato, F., Verda, V., Santarelli, M., Sciacovelli, A., 2017. CSP plants with thermocline thermal energy storage and integrated steam generator – Techno-economic modeling and design optimization. Energy 139, 231–246. doi:10.1016/j.energy.2017.07.160

Rivas, E., Rojas, E., Bayón, R., Gaggioli, W., Rinaldi, L., Fabrizi, F., 2014. CFD model of a molten salt tank with integrated steam generator. Energy Procedia 49, 956–964. doi:10.1016/j.egypro.2014.03.103

Rosen, M.A., 2001. The exergy of stratified thermal energy storages. Sol. Energy 71, 173–185. doi:10.1016/S0038-092X(01)00036-6

Siemens, 2021. Star-CCM+ [WWW Document]. URL https://www.plm.automation.siemens.com/global/en/products/simcenter/STAR-CCM.html

Turchi, C.S., Boyd, M., Kesseli, D., Kurup, P., Mehos, M., Neises, T., Sharan, P., Wagner, M., Wendelin, T., 2019. CSP System Analysis - Final Project Report - NREL/TP-5500-72856.

World Energy Council, 2013. World Energy Resources: Solar [WWW Document]. URL https://www.worldenergy.org/assets/images/imported/2013/10/WER_2013_8_Solar_revised.pdf

Xu, C., Li, X., Wang, Z., He, Y., Bai, F., 2013. Effects of solid particle properties on the thermal performance of a packed-bed molten-salt thermocline thermal storage system. Appl. Therm. Eng. 57, 69–80. doi:10.1016/j.applthermaleng.2013.03.052